



# Investigation of Pyrolysis Characteristics and Product Evolution Behavior of Methyl Oleate under the Effect of Copper Slag

Yaohuan Wang<sup>1,2,3</sup> · Fengxia Zhang<sup>1,2,4</sup> · Jianhang Hu<sup>1,2,3</sup> · Shiliang Yang<sup>1,2,3</sup> · Huili Liu<sup>1,2,3</sup> · Hua Wang<sup>1,2,3</sup>

Received: 2 January 2024 / Accepted: 27 March 2024 / Published online: 9 May 2024

© The Author(s), under exclusive licence to Springer Science+Business Media, LLC, part of Springer Nature 2024

## Abstract

Biodiesel is a highly potential energy source with the characteristics of renewability and environmental friendliness. In this study, methyl oleate (MO, unsaturated fatty acid) was selected as a model compound for biodiesel. The thermal conversion behavior of MO and the reaction characteristics of copper slag (CS) catalytic pyrolysis of MO were investigated. The thermal conversion behavior of MO was explored by Py-GC/MS and TG-FTIR. The results showed that the pyrolysis products of MO mainly consisted of oxygenated compounds, alkenes, alkanes, and aromatics. Furthermore, the final product of the catalytic pyrolysis of MO by CS was analyzed. More gas products were produced under the effect of CS. The components of the gas products were determined by gas chromatography (GC). The results revealed that CS promoted the production of H<sub>2</sub> and CO. The coke was analyzed and characterized by FTIR, Raman and SEM. The addition of CS enhanced the decomposition of oxygen-containing structures, leading to the change of particle size and chemical structure of coke. The research contributes to understanding the thermal conversion behavior of unsaturated fatty acids and the reaction characteristics under the effect of CS. This provides valuable information for the application of biodiesel to replace fossil energy in the copper smelting process.

**Keywords** Methyl oleate · Copper slag · Pyrolysis · Product characteristics

## 1 Introduction

The significant increase in the demand for fossil energy and the environmental problems it brings, the development of renewable and low-carbon energy sources has been promoted. Based on a survey, the continued use of fossil energy will cause the growth of carbon emissions to 33 Gt by 2040 [1]. Meanwhile, fossil energy sources are being rapidly depleted, with oil and natural gas predicted to run out in half

a century [2]. Therefore, the transition to sustainable and clean energy is becoming increasingly important. Biodiesel, as a green energy source, has remarkable advantages such as renewability, carbon neutrality and low sulfur content [3], which is a type of biomass fuel with promising prospects for development.

Biodiesel generally refers to a biomass fuel made from renewable energy by transesterification reaction [4]. In recent years, the primary raw materials used to produce biodiesel have been canola oil, jatropha curcas oil, and waste cooking oil [5]. Despite the variety of raw material sources, the main components are methyl palmitate, methyl oleate and methyl linoleate [6]. The application of biodiesel in engines has been shown to significantly decrease the emissions of pollutants, including carbon monoxide, hydrocarbons and particulate matter [7, 8]. Nonetheless, the use of biodiesel can lead to the production of coke and nozzle clogging, causing machine damage and hindering the promotion and application of biodiesel [9]. Furthermore, relevant explorations have been conducted by researchers on catalytic cracking of biodiesel into hydrocarbon-rich fuels [10, 11]. But this method is more costly and less economical. Therefore, exploring the application of biodiesel in other fields can not only reduce the emission of

✉ Jianhang Hu  
jianhang@kust.edu.cn; hujh51@126.com

<sup>1</sup> Engineering Research Center of Metallurgical Energy Conservation and Emission Reduction, Ministry of Education, Kunming University of Science and Technology, Kunming 650093, China

<sup>2</sup> State Key Laboratory of Complex Nonferrous Metal Resources Clean Utilization, Kunming University of Science and Technology, Kunming 650093, China

<sup>3</sup> Faculty of Metallurgical and Energy Engineering, Kunming University of Science and Technology, Kunming 650093, China

<sup>4</sup> Kunming Metallurgy College, Kunming 650093, China

greenhouse gases, but also contribute to breaking through the limitations of biodiesel application.

The CO<sub>2</sub> emissions generated by the non-ferrous metals industry account for more than 8% of the country's total CO<sub>2</sub> emissions, and have the possibility of continuing to increase [12]. As the largest producer and consumer of non-ferrous metal industrial products [13], China is facing a huge problem of energy consumption and carbon emissions. In 2022, China produced 11.063 million tons of refined copper, accounting for 43.1% of the world's copper production, and has significant potential for energy conservation and emission reduction. Currently, biomass fuels such as pine sawdust, walnut shells and waste cooking oil have been explored for use in the copper smelting industry, which has a significant effect on reducing carbon emissions [14, 15]. However, the application of biomass fuels in the copper smelting process can be affected by the copper slag (CS) in the melting pool. The main components of CS are fayalite (Fe<sub>2</sub>SiO<sub>4</sub>), magnetite (Fe<sub>3</sub>O<sub>4</sub>) and a small amount of residual copper [16]. Du et al. [17] investigated the evolution of pyrolysis products of rubber seed oil using CS as a catalyst. The yield of gas and coke increased significantly in the presence of CS, while the tar yield decreased. Dong et al. [18] found that carbon conversion and gas yield of sewage sludge could be effectively improved by modifying CS. The studies also found that Fe<sub>2</sub>SiO<sub>4</sub> can promote the cracking of tar to improve the quality of gas production [19]. The Fe<sub>3</sub>O<sub>4</sub> can provide more lattice oxygen for the pyrolysis gasification reaction, thereby producing a greater amount of syngas [20]. Therefore, conducting intensive research on the product evolution of biomass fuel pyrolysis process under the effect of CS is beneficial to the efficient utilization of biomass fuel.

In this study, MO was selected as a model compound for biodiesel for the purpose of studying the thermal conversion behavior of MO and analyzing the formation mechanism of pyrolysis products of MO under the catalysis of CS. First, the thermal transformation behavior of MO was examined through Py-GC/MS and TG-FTIR. The components of pyrolysis products were determined by Py-GC/MS at different temperatures. The transformation process from macromolecular to small molecular compounds and the changes of intermediates were analyzed. TG-FTIR was used to determine the pyrolysis behavior and the evolution of volatiles. Then, the products of catalytic pyrolysis of MO by CS were investigated. The changes in the gas products were analyzed by GC. The coke was analyzed and characterized using FTIR, Raman, and SEM. The conclusions of this work are favorable to break through the limitations of biodiesel application. Meanwhile,

new insights are provided to promote sustainable development in the non-ferrous metals industry.

## 2 Materials and Methods

### 2.1 Materials

MO (≥ 99%) was used as a feedstock to replace biodiesel for the study. The chemical formula of MO is C<sub>19</sub>H<sub>36</sub>O<sub>2</sub>. Low temperature (2–8 °C) storage is used to maintain its physicochemical properties. Furthermore, the CS in this study was obtained from Yunnan Copper Co., Ltd. The CS was crushed into particle samples less than 0.75 mm in diameter for subsequent use. Table 1 reveals that CS contains 33.06 wt.% Fe, 17.82 wt.% Cu, 19.13 wt.% SiO<sub>2</sub> and 7.03 wt.% (CaO + Al<sub>2</sub>O<sub>3</sub> + MgO). The X-ray diffraction (XRD) pattern shows that CS is primarily composed of Fe<sub>3</sub>O<sub>4</sub>, Fe<sub>2</sub>SiO<sub>4</sub> and Cu<sub>2</sub>S phases, and the results can be seen in Fig. 1.

### 2.2 Methods

The CS was dried at 105 °C for 24 h prior to the pyrolysis experiments. MO was used as received. Pyrolysis experiments of MO were carried out in a vertical tube furnace, and

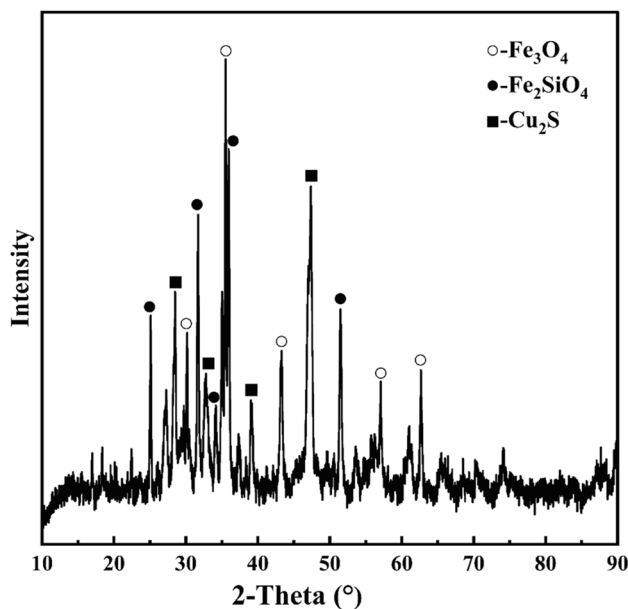


Fig. 1 XRD pattern of CS

**Table 1** Compositional of CS samples (wt.%)

Fe(total)	Cu	SiO <sub>2</sub>	CaO	S	Al <sub>2</sub> O <sub>3</sub>	MgO	Fe <sub>3</sub> O <sub>4</sub>	ZnO
33.06	17.82	19.13	2.12	8.07	2.96	1.95	12.90	1.83

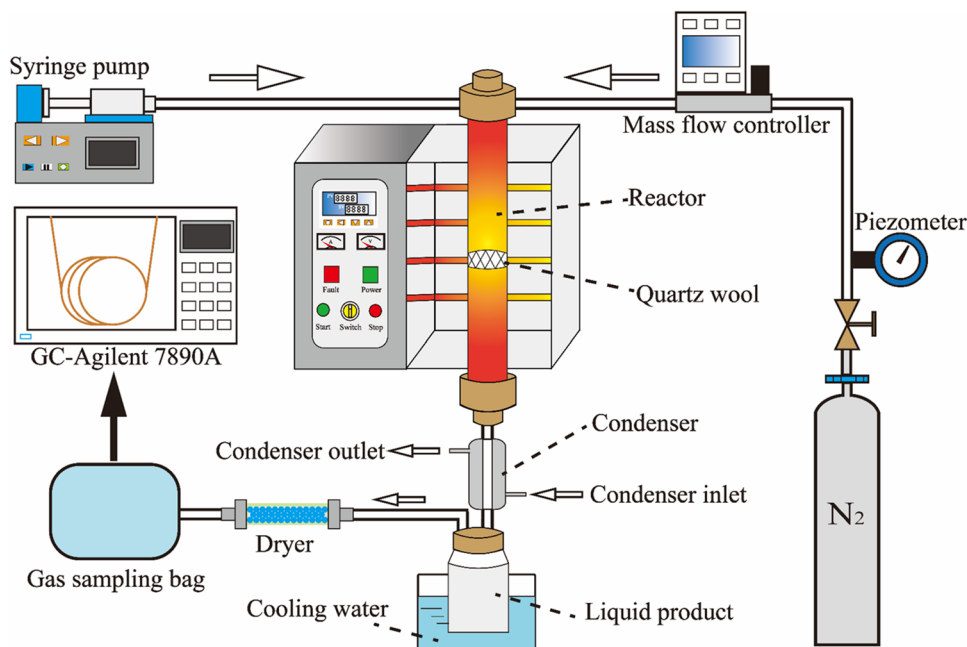
the furnace temperature stability was maintained within  $\pm 2$  °C. Liquid samples (MO) were injected into the reactor through a liquid syringe pump at an injection rate of 0.05 mL/min. Quartz wool (3–5  $\mu\text{m}$  in diameter) was loaded from the bottom to the middle of the reactor in order to easily collect of coke from pyrolysis. Meanwhile, quartz wool can also be used as a filler to secure CS (0.5 g) in the center of the reactor. Nitrogen was used as a carrier gas to ensure that the reaction was conducted in an inert atmosphere. The pipes were connected according to Fig. 2 and checked for airtightness of the individual interfaces. Before the experiment started, the reactor was purged with  $\text{N}_2$  (flow rate 30 mL/min, purge time 10 min) to ensure that no other gases were retained in the reactor. At the end of purging, the flow rate of  $\text{N}_2$  was adjusted to 10 mL/min. Then, the tube furnace was heated to the experimental temperature (950–1150 °C). When the experimental temperature was reached, the syringe pump was turned on to inject the liquid samples into the reactor. The injection amount was 2.5 g each time. Finally, the liquid products were cooled by a condenser and collected in glass bottles. The gas products were further dried and filtered out, and then collected in gas sampling bags.

### 2.3 Characterization

The composition and elemental content of CS were measured using chemical analysis and ICP-OES. The mineralogical composition of CS was determined by X-ray diffraction (XRD, RIGAKUTTRIII-18KW). Measurement was made from 10° to 90° using  $\text{Cu-K}\alpha$  radiation at 0.02° intervals and a step size of 10°/min. The products of rapid pyrolysis from MO were analyzed by Py-GC/MS. The

pyrolysis experiments were performed in the pyrolyzer model EGA/PY-3030D, while the analysis of volatiles from the pyrolysis was carried out in a GC/MS (QP2020 NX, SHIMADZU). Before conducting the experimental test, 0.5  $\mu\text{L}$  of the sample was injected into a crucible using a micro syringe and the crucible loaded with the sample was filled with quartz wool. Then, the prepared sample was placed into the sampler. When the pyrolyzer was heated to the specified temperature (500–900 °C), the sample was pushed into the pyrolyzer for pyrolysis with a residence time of 0.2 min. The pyrolysis products were transported to the GC/MS by high-purity He (flow rate: 1 mL/min and split ratio: 60:1). The GC capillary column was Shimadzu SH-I-5SiI MS (60 m  $\times$  0.25 mm  $\times$  0.25  $\mu\text{m}$ ). The interface temperature, ion source temperature and inlet port temperature were 300 °C, 280 °C and 320 °C. The scanning mass range of mass spectrometer was 45–600 (m/z). The heating program for the column oven was set to: (1) holding at 40 °C for 2 min. (2) heating from 40 °C to 150 °C at a heating rate of 5 °C/min and holding for 8 min. (3) heating from 150 °C to 210 °C at a heating rate of 10 °C/min and holding for 5 min. (4) heating from 210 °C to 280 °C at a heating rate of 5 °C/min and holding for 3 min. The chromatographic peaks obtained by pyrolysis can be identified according to the NIST MS database. The relative amount of pyrolysis products can be determined by calculating the ratio of peak areas for individual compounds to the total peak area. The evolution behavior of the volatiles from the pyrolysis of MO was investigated by TG-FTIR (TG: TG2, Mettler; FTIR: Nicolet iS50, Thermo Fisher Scientific). The sample of 15 mg was heated from 30 °C to 800 °C (heating rate: 10 °C/min) under  $\text{N}_2$  atmosphere.

**Fig. 2** Schematic flow of pyrolysis experiment



Then, the volatiles were purged through N<sub>2</sub> to the infrared spectrometer. To prevent condensation, the temperature of the transfer line was maintained at 250 °C all the time.

Gas components and contents were determined by a gas chromatograph (GC-Agilent 7890A). The chromatographic columns used were HP-PLOT/Q (to separate C<sub>2</sub>H<sub>2</sub>, C<sub>2</sub>H<sub>4</sub>, C<sub>2</sub>H<sub>6</sub> and CO<sub>2</sub>) and HP-MOLESIEVE (to separate H<sub>2</sub>, CH<sub>4</sub>, CO and N<sub>2</sub>), respectively. The column oven temperature was maintained for 5 min after reaching 50 °C, then heated to 150 °C (20 °C/min) and held for 6 min. The gas products were transported to the chromatographic column using Ar. The functional group structure of coke was determined by Fourier transform infrared spectroscopy (FTIR, NICOLET iS50). The experimental test was performed using the potassium bromide pellet method. The range of testing was 500–4000 cm<sup>-1</sup>. The molecular structural information of coke was detected using a Raman spectrometer (Raman, Renishaw inVia reflex). Raman data were collected a scanning range of 500 to 2500 cm<sup>-1</sup>. The laser power of the excitation source was 5 mw. The excitation wavelength and spectral resolution were 532 nm and 4 cm<sup>-1</sup>. At the voltage of 10 kV and under high vacuum pattern, the microscopic morphology of coke was analyzed by scanning electron microscope (Quanta FEG 250).

## 2.4 Calculation of Pyrolysis Products

During the pyrolysis process, the yield of liquid products and coke can be defined according to Eqs. (1) and (2). The gas products are obtained by mass balance calculations as shown in Eq. (3).

$$Y_{Liquid} = \frac{m_{Liquid}}{m_{Sample}} \times 100\% \quad (1)$$

$$Y_{Coke} = \frac{m_{Coke}}{m_{Sample}} \times 100\% \quad (2)$$

$$Y_{Gas} = 1 - Y_{Liquid} - Y_{Coke} \quad (3)$$

where  $m_{Liquid}$ ,  $m_{Coke}$  and  $m_{Gas}$  are the masses of the liquid products, coke and gas products, respectively.  $m_{Sample}$  is the mass of the sample.

The volume fraction of each gas component was determined by GC in the gas product, and the obtained data can be used to calculate the yield of each gas with the following formula:

$$Y_i = \frac{q_{N_2} x_i t_{injection}}{x_{N_2} m_{sample}} \quad (4)$$

where  $Y_i$  is the yield of different gas components (H<sub>2</sub>, CH<sub>4</sub>, C<sub>2</sub>H<sub>2</sub>, C<sub>2</sub>H<sub>4</sub>, C<sub>2</sub>H<sub>6</sub>, CO and CO<sub>2</sub>).  $q_{N_2}$  and  $x_{N_2}$  are the mass

flow rate and volume fraction of N<sub>2</sub>, respectively.  $t_{injection}$  is the injection time.  $x_i$  is the volume fraction of component  $i$ .

## 3 Results and Discussion

### 3.1 Analysis of the Rapid Pyrolysis Characteristics of MO

To clarify the product transformation regulation and formation mechanism of MO during pyrolysis, the components of the pyrolysis products were determined using Py-GC/MS. The transformation process from macromolecular compounds to small molecular compounds and the changes of intermediate products were analyzed. The evolution behavior of the functional groups of volatiles during pyrolysis was detected using TG-FTIR.

#### 3.1.1 Py-GC/MS Analysis

The information of the identifiable pyrolysis product in the total ion chromatogram is listed in Table S1. The identified compounds contained oxygenated compounds, alkenes, alkanes and aromatics. It can be seen from Fig. 3 that the relative content of pyrolysis products changed remarkably at different temperatures. At 500 °C, only oxygenated compounds (99.87%) and alkenes (0.12%) were detected in the pyrolysis products, while alkanes and aromatics were not detected. The oxygenated compounds were mainly dominated by methyl palmitate (21.59%), methyl oleate (65.68%) and methyl stearate (9.03%). When the temperature was increased to 600 °C, the overall change in the pyrolysis components was not significant. In the range of 700–800 °C, the content

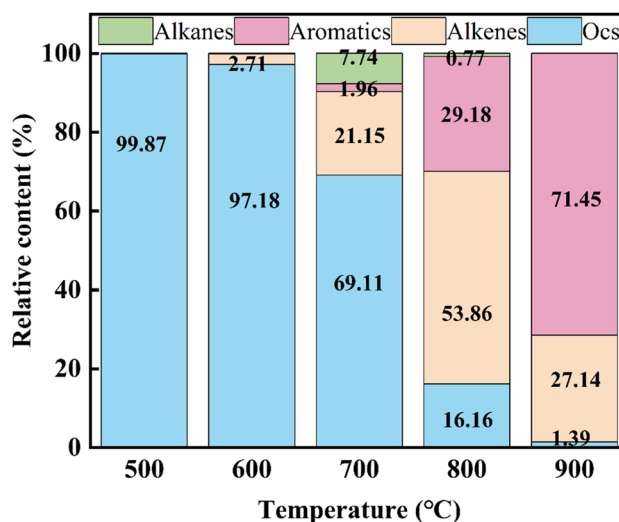
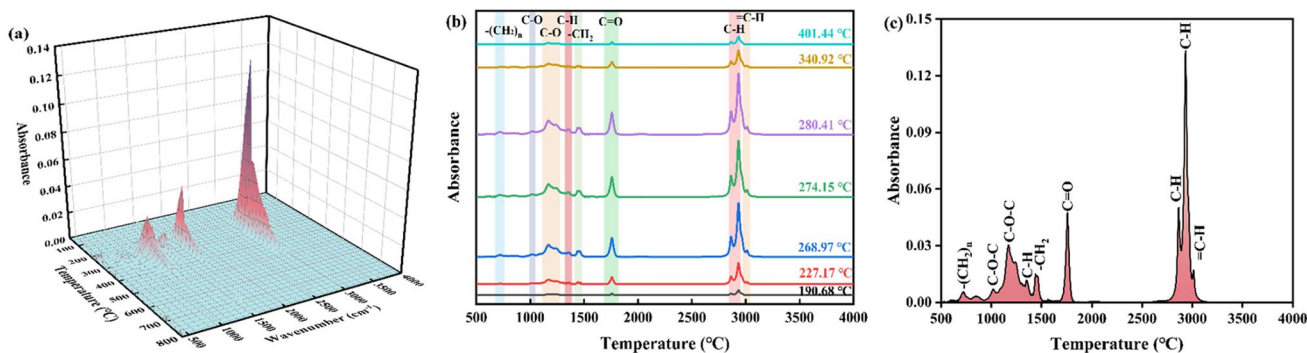


Fig. 3 Effect of temperature on the content of pyrolysis products

of oxygenated compounds decreased significantly from 69.11% to 16.16%. The contents of alkenes and aromatics increased with the increase of temperature, reaching 53.86% and 29.18% at 800 °C, respectively. As the temperature was further increased, aromatics were the most abundant pyrolysis products, which accounted for 71.45% of the total content. Nevertheless, the other three categories of products showed a decreasing trend. Aromatics can be divided into monocyclic aromatics (MAHs) and polycyclic aromatics (PAHs). The aromatics in the pyrolysis products of MO are primarily consist of MAHs, including 41.07% benzene, 10.9% toluene and 7.43% styrene. The above results indicate that only preliminary pyrolysis of MO was performed at lower temperatures, and no decarboxylation reaction occurred. A similar phenomenon was found in the pyrolysis experiments of hydrogenated palm oil by Xu et al. [21]. With the increase in temperature, oxygenated compounds undergo reactions such as decarboxylation and decarbonylation to form alkenes and alkanes. Meanwhile, the higher temperature enhances the dehydrogenation reaction, resulting in the conversion of long-chain alkenes into short-chain alkenes. When the temperature is increased again, alkenes and alkanes are further formed into aromatics through cyclization, Diels–Alder reaction and dehydrogenation [22].

### 3.1.2 TG-FTIR Analysis

The change characteristics of the pyrolysis products of MO were analyzed in real time by TG-FTIR, as shown in Fig. 4. Table 2 summarizes the characteristic absorption bands of specific gases and functional groups in the volatiles from MO pyrolysis and Fig. S1 presents the TG-DTG curves for the pyrolysis process of MO. The maximum mass loss was 21.79 wt.% during pyrolysis of MO, corresponding to a temperature of 268.97 °C. A significant change was observed in the infrared absorption peaks when the pyrolysis temperature ranged from 190.68 °C to 401.44 °C (see Fig. 4(b)). The presence of smaller absorption peaks in the infrared spectrum at 190.68 °C indicates that MO has started to volatilize at this temperature. The band at 3040–3010  $\text{cm}^{-1}$  corresponds to =C-H stretching, which derives from alkene group. The antisymmetric and symmetric stretching vibrations of C-H are located at 2933  $\text{cm}^{-1}$  and 2864  $\text{cm}^{-1}$ , which are mainly described by the presence of aliphatic in  $\text{CH}_2$  and terminal  $\text{CH}_3$  groups in the volatiles. The band at 1900–1600  $\text{cm}^{-1}$  corresponds to C=O stretching, indicating the presence of esters and carboxylic acids in the volatiles [23]. As the temperature increased to 224.1 °C, the absorption peaks observed at 1490–1350  $\text{cm}^{-1}$  belong to  $-\text{CH}_2$  bending vibration, which



**Fig. 4** TG-FTIR of MO pyrolysis at 10 °C/min: **a** 3D FTIR. **b** FTIR at different temperatures. **c** FTIR at the maximum absorption peak

**Table 2** The characteristic absorption bands in pyrolysis volatiles [25, 26]

Wavenumber( $\text{cm}^{-1}$ )	Peak ( $\text{cm}^{-1}$ )	Assignment	Possible species
3040–3010	3016	=C-H stretching vibration	Alkene group
3000–2843	2933, 2864	C-H antisymmetric and symmetric stretching	aliphatic in $\text{CH}_2$ and terminal $\text{CH}_3$ group
1900–1600	1758	C=O stretching	Ketones, Aldehydes, Esters, Carboxylic acids
1490–1350	1440	$-\text{CH}_2$ bending vibration	Alkanes group
1380–1330	1351	C-H bending vibration	$\text{CH}_2$ and $\text{CH}_3$ aliphatic group
1300–950	1170, 1024	C–O–C stretching	Ethers, Alcohols, Phenols
730–630	720	$-(\text{CH}_2)_n$ rocking vibration	long chain hydrocarbon



is mainly attributed to the alkanes group. The band located at 1380–1330  $\text{cm}^{-1}$  is related to the C-H bending vibration, with the main contributions deriving from the  $\text{CH}_2$  and  $\text{CH}_3$  aliphatic groups. The absorption peaks appeared at 1300–950  $\text{cm}^{-1}$  corresponding to the C–O–C stretching of alcohols, ethers and phenols. Additionally, there is an inconspicuous absorption peak at 730–630  $\text{cm}^{-1}$ . This is a characteristic peak for long chain fatty acids and represents the  $-(\text{CH}_2)_n$  rocking vibration process [24]. The absorbance reached a maximum at 280.41  $^\circ\text{C}$  with further increases in temperature. Then, the absorption peak basically disappeared at 401.44  $^\circ\text{C}$ . It is noteworthy that the absorbance is not at its maximum at 268.97  $^\circ\text{C}$  (maximum mass loss temperature). This may be attributed to delayed phenomena generated by the transfer of volatiles in the TGA furnace and their detection in the FTIR. A similar phenomenon was found during the study of heavy fuel oil pyrolysis by Abdul et al. [25].

### 3.2 Distribution Characteristics of Catalytic Pyrolysis Products

Figure 5 illustrates the distribution characteristics of the pyrolysis products of MO at different temperatures and catalyzed by CS. As shown in Fig. 5(a), the coke yield increased to 69.26 wt.% and the gas yield decreased to 30.74 wt.% with the increase of temperature (from 950  $^\circ\text{C}$  to 1150  $^\circ\text{C}$ ). The production of liquid products was observed only at 950  $^\circ\text{C}$  and 1000  $^\circ\text{C}$ . The results indicate that high temperatures can accelerate the pyrolysis of liquid products and favor the generation of gas products and coke. Meanwhile, it was observed that a significant amount of coke was produced during the pyrolysis process. The reason is that as an unsaturated fatty acid, MO has a higher degree of unsaturation, the pyrolysis process is more tend to produce aromatic compounds. Moreover, the breaking of the C–C bond in MO

contributes to the formation of dienes and alkenes [27]. The Diels–Alder reaction and dehydrogenation subsequently occur, resulting in the formation of aromatic compounds. The aromatic compounds can further form coke through cyclization and polymerization reactions. With the addition of CS, it can be observed that gas products significantly increased, while coke gradually decreased (see Fig. 5(b)). The CS contains active metal ions such as Cu, Fe, Ca, Al, Mg and Zn. These metal ions have a catalytic effect and can promote the pyrolysis reaction [28, 29]. The catalytic effect of CS becomes increasingly evident as the temperature increases, which is favorable to the conversion of MO into gas products. To better understand the catalytic role of CS, it is necessary to further analyze the gas products and coke in subsequent sections.

### 3.3 Variation Properties of Gas Products

The main components of gases from the pyrolysis of MO are  $\text{H}_2$ ,  $\text{CH}_4$ ,  $\text{CO}$ ,  $\text{CO}_2$  and C2 gases (such as  $\text{C}_2\text{H}_2$ ,  $\text{C}_2\text{H}_4$ ,  $\text{C}_2\text{H}_6$ ). Figure 6 shows the yields of various components in the gas products of pyrolysis. In Fig. 6 (a–c), the yield of C2 gases gradually decreased with increasing temperature and decreased to 0.68 mL/g ( $\text{C}_2\text{H}_2$ ), 1.89 mL/g ( $\text{C}_2\text{H}_4$ ), and 3.28 mL/g ( $\text{C}_2\text{H}_6$ ), respectively. Due to the high temperatures that promote the dehydrogenation reaction and the Diels–Alder reaction, more hydrocarbons are converted into aromatics, resulting in a decrease in their yields [30]. Subsequently, the aromatics further formed coke, which is consistent with the phenomenon of increased coke yield in Sect. 3.2. The yield of C2 gases in MO exhibited a decreasing trend under the effect of CS. CaO in CS promotes condensation reactions (such as aldehydes and ketones), which results in a decrease of olefinic compounds decomposed into C2 gas [31]. Fe can promote the breaking of C–C and C–H bonds [32], causing the decomposition of C2 gas into carbon and hydrogen

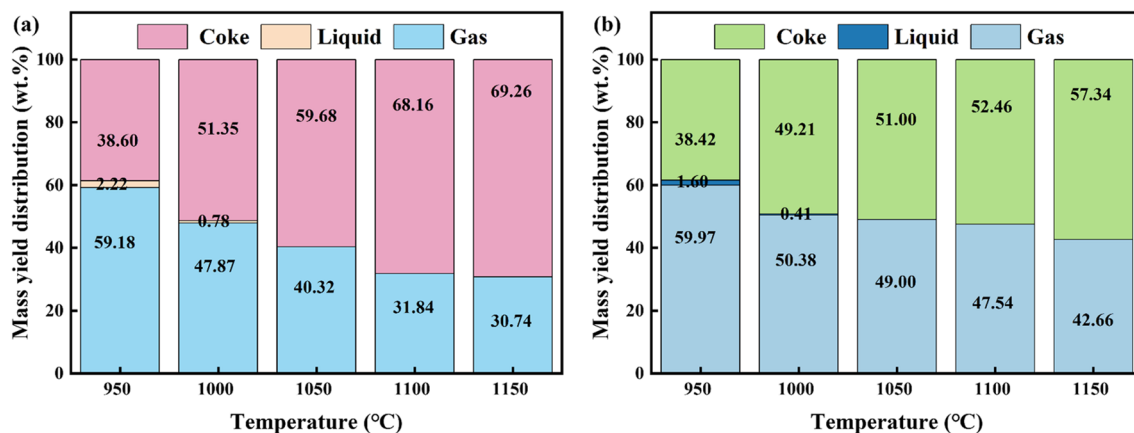
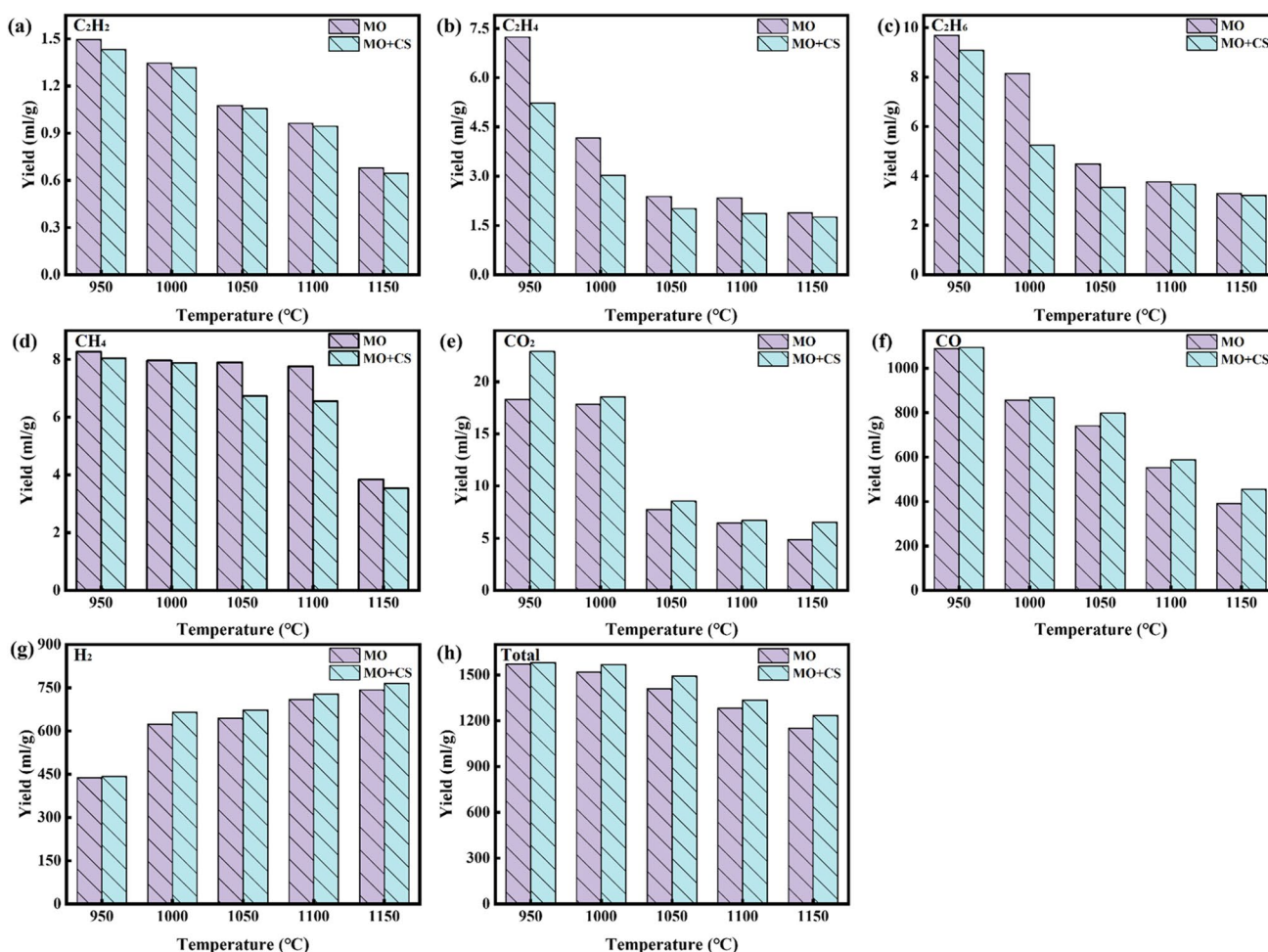


Fig. 5 Pyrolysis products distribution of MO at different temperatures: a without CS. b with CS



**Fig. 6** Variation of gas yield of MO under different conditions

under high temperature conditions. When the temperature was increased from 950 °C to 1150 °C, the yield of CH<sub>4</sub> and CO<sub>2</sub> from the pyrolysis of MO decreased from 8.27 mL/g and 18.30 mL/g to 3.84 mL/g and 4.86 mL/g. The reason is that high temperatures (> 900 °C) promote the cracking of CH<sub>4</sub> [33]. The decrease in CO<sub>2</sub> yield may be due to the Boudouard reaction that occurs during the pyrolysis process. Metal oxides (MgO, ZnO) in CS can accelerate the breaking of C–C and C–H bonds [34], thereby reducing CH<sub>4</sub> yield. Whereas CaO can promote the decarboxylation reaction, which increases the yield of CO<sub>2</sub>.

It can be observed from Fig. 6 (f, g) that a significant quantity of CO and H<sub>2</sub> is present in the gas products. When the pyrolysis temperature was increased, the yield of CO in MO decreased from 1088.99 mL/g to 392.10 mL/g, while the yield of H<sub>2</sub> increased from 437.82 mL/g to 742.98 mL/g. CO is produced by the decomposition and reformation of C=O and COO groups. The H<sub>2</sub> is mainly derived from the dehydrogenation of hydrocarbons, the reformation of aromatic C=C and C–H groups [35]. The formation of large

amounts of CO and H<sub>2</sub> is primarily attributed to the secondary cracking of the liquid products. The yield of both CO and H<sub>2</sub> increased under the influence of CS. The reason is that Fe<sup>3+</sup> and Cu in CS promote the decarbonylation reaction, resulting in an increase in CO yield [36, 37]. Alkaline oxides, Cu and Fe accelerated the dehydrogenation reaction, which facilitated the production of H<sub>2</sub>. Furthermore, the addition of CS also promoted an increase in the total gas yield, which is consistent with the results analyzed of Fig. 5.

### 3.4 Analysis and Characterization of Coke

#### 3.4.1 FTIR and Raman Analysis of Coke

The FTIR of two types of coke produced by the pyrolysis of MO at different temperatures is shown in Fig. 7. Table S2 displays the types of functional groups corresponding to the different wave numbers. The results revealed that the absorption peaks of the two types of coke exhibited good consistency, but the intensity of each absorption peak was

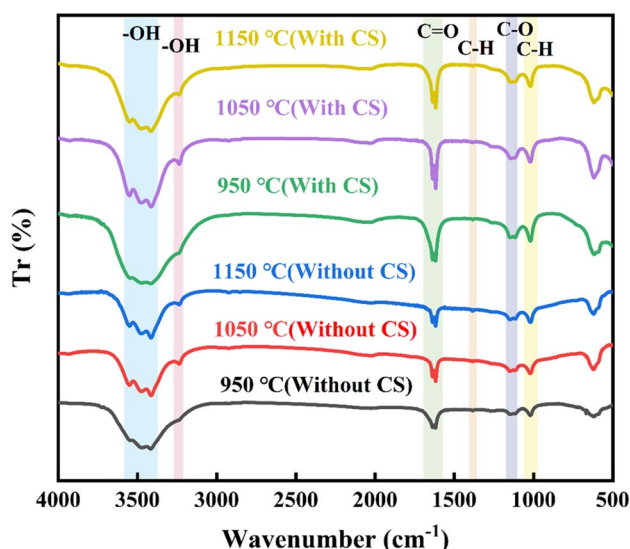


Fig. 7 FTIR of two types of coke at different temperatures

different. The peaks at  $3550\text{--}3400\text{ cm}^{-1}$  and  $3236\text{ cm}^{-1}$  correspond to the  $\text{-OH}$  stretching vibrations of the intramolecular hydrogen-bonded hydroxyl group and the intermolecular hydrogen-bonded hydroxyl group, respectively. The peak at  $1618\text{ cm}^{-1}$  belongs to the  $\text{C}=\text{O}$  stretching vibration conjugated to the aromatic ring. The  $\text{C-H}$  asymmetric deformation ( $1385\text{ cm}^{-1}$ ) is related to  $\text{-CH}_3$  and  $\text{-CH}_2\text{-}$ . Besides these assignments, the symmetric  $\text{C-O}$  stretching of  $\text{C-O-C}$  in aromatic rings is identified at a bandwidth of  $1134\text{ cm}^{-1}$ . And at  $1020\text{ cm}^{-1}$  is the aromatic  $\text{C-H}$  deformation. The  $\text{-OH}$  stretching vibration decreased with increasing temperature for the reason that high temperature promotes the depolymerization and dehydration process of MO [38].

Furthermore, functional groups such as  $\text{C-O}$ ,  $\text{C}=\text{O}$  and  $\text{-OH}$  were observed in coke. This is because oxygen-containing compounds can accelerate the formation of coke during pyrolysis, resulting in more oxygen-containing functional groups being fixed in coke [17]. The functional group structure of coke did not change under the effect of CS. With the addition of CS, the intensity of peaks at  $\text{C}=\text{O}$ ,  $\text{C-H}$ , and  $\text{C-O}$  increased, indicating that CS promoted the cracking of oxygen-containing compounds.

Raman is commonly applied to determine the ordered and disordered character of the structure of carbon material. The study examined the impact of CS and temperature on the microstructure of coke through Raman. In Figs. 8(a) and (e), it is evident that there are two distinct vibrational regions in the first-order region of the Raman spectrum, which are the D band and the G band. However, there is a significant amount of overlapping structural information in the D band and G band peaks [39]. To obtain more precise structural information, this paper deconvolutes the first-order Raman spectra into five bands: the S band, D band, V band, G band, and  $\text{G}_L$  band. The positions corresponding to each band are shown in Table S3. The area of each peak can be obtained based on the result of the deconvolution and is shown in Fig. 9(a). The total Raman area ( $I_{\text{all}}$ ) declined as the temperature increased, indicating a reduction in the amount of oxygen-containing functional groups in the coke [40]. The  $I_{\text{all}}$  decreased under the influence of CS. The reason is probably that CS promotes the cracking of oxygen-containing functional groups in the coke. The G band derives from the  $\text{sp}^2$ -bonded carbon structure and is widely present in highly ordered carbon materials, representing the degree of graphitization of the carbon material [40]. The D band is associated with disorder around the  $\text{sp}^2$  carbon, indicating the

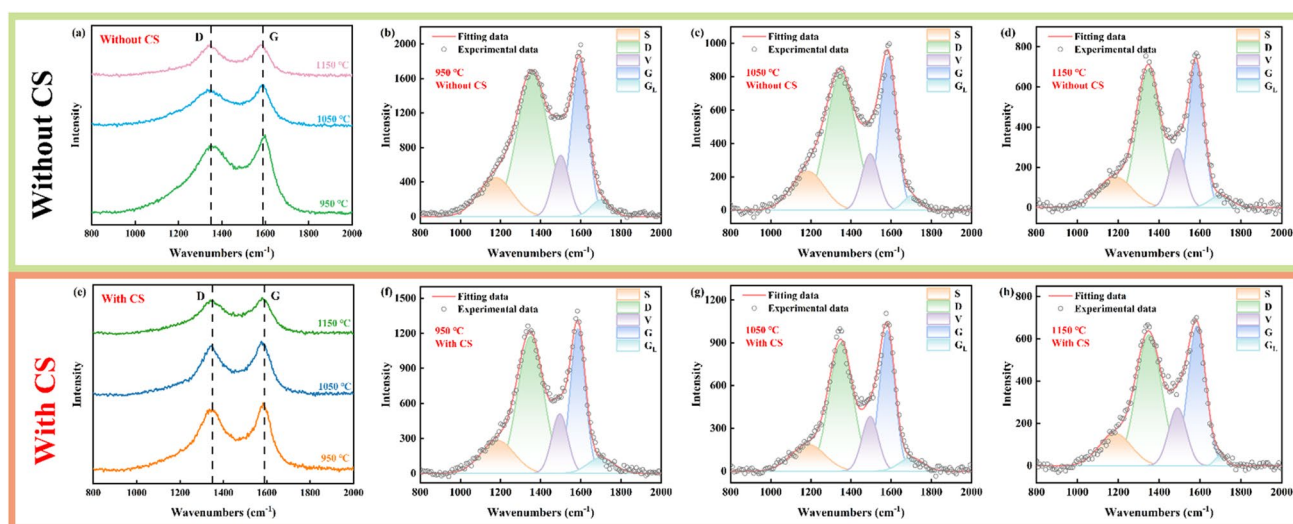
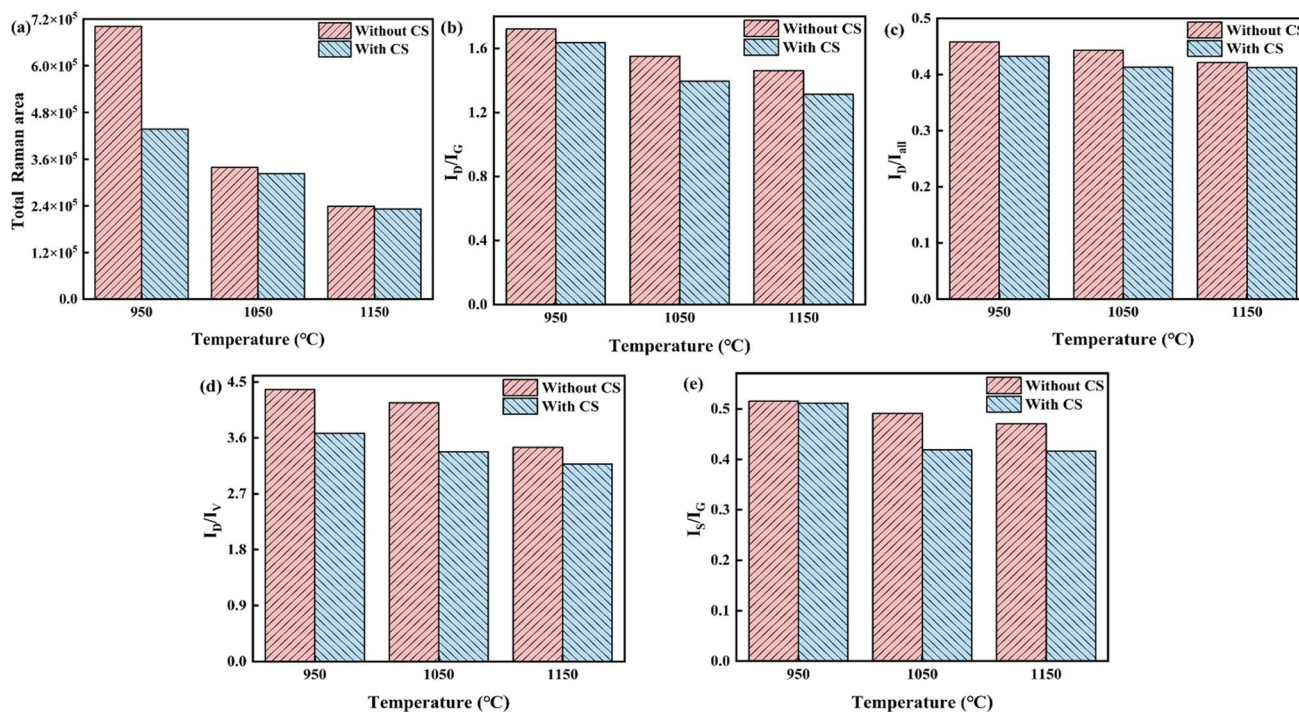


Fig. 8 Raman spectra of coke under different conditions: a–d without CS. e–h with CS





**Fig. 9** The area ratio of the fitted band: **a** Total Raman area. **b**  $I_D/I_G$ . **c**  $I_D/I_{all}$ . **d**  $I_D/I_V$ . **e**  $I_S/I_G$

presence of multiple ( $\geq 6$ ) benzene rings [17]. The degree of graphitization in carbon materials can be expressed by the  $I_D/I_G$  ratio. The ratio of  $I_D/I_G$  decreased from 1.72 to 1.46 as the temperature increased, as shown in Fig. 9(b). This indicates that a decrease in the proportion of defective or edge-bonded aromatic ring structure, enabling the graphitization of coke to increase [41]. The addition of CS resulted in a decrease in the ratio of  $I_D/I_G$ , indicating that CS promotes the conversion of the amorphous carbon structure to an ordered graphite-like structure. The decrease in the ratio of  $I_D/I_{all}$  also illustrates this point. However, this does not demonstrate that the coke has transformed into graphitic crystals. The reason is that the presence of a relatively wide bandwidth in the D band indicates the containing of aryl rings of varying sizes in the coke [42].

The  $I_D/I_V$  ratio is an important parameter for measuring the change in the number of small and large rings in coke. The S band is associated with  $sp^3$ -rich carbon structures and represents a measure of substituents (C–C structure between alkyl and aryl, methyl carbons hanging from the aromatic ring) and crosslinking densities [43]. As can be seen from Fig. 9(d) and Fig. 9(e), the ratio of  $I_D/I_V$  and  $I_S/I_G$  both exhibited a decreasing trend with increasing temperature. The decrease in the ratio of  $I_D/I_V$  is probably attributed to the consumption of larger aromatic rings and/or conversion into smaller aromatic rings. High temperatures promote the cracking of oxygen-containing functional groups, which leads to the decomposition of larger oxygen-containing

aromatic rings into smaller structures. Furthermore, the decrease in the total Raman area also confirms that high temperatures favor the cracking of oxygen-containing functional groups. The ratio of  $I_D/I_V$  decreased with the addition of CS, indicating that the presence of CS may enhance the release of oxygen-containing functional groups. However, the overall change trend of the  $I_S/I_G$  ratio is very small, regardless of whether CS is added or not. This demonstrates that the S band structure is not easily eliminated, but will persist in the coke along with the aromatic structures.

### 3.4.2 SEM Analysis of Coke

The microscopic morphology of coke can be observed using scanning electron microscopy (SEM). Figure 10 illustrates the SEM images and the corresponding particle size distribution of coke derived from MO pyrolysis at different temperatures. The coke obtained from pyrolysis mainly consists of an accumulation of small spherical particles of different sizes and exhibits a similar shape (coral-like). The pyrolysis process at high temperature is mainly dominated by gas-phase volatiles. And the gas-phase volatiles can generate small particles through secondary reaction [17], so that the images observed by SEM are basically small spherical particles. However, the shape of coke did not undergo much change under the effect of CS and still remained as spherical particles (Fig. 11 (a-c)). The results indicated that the formation

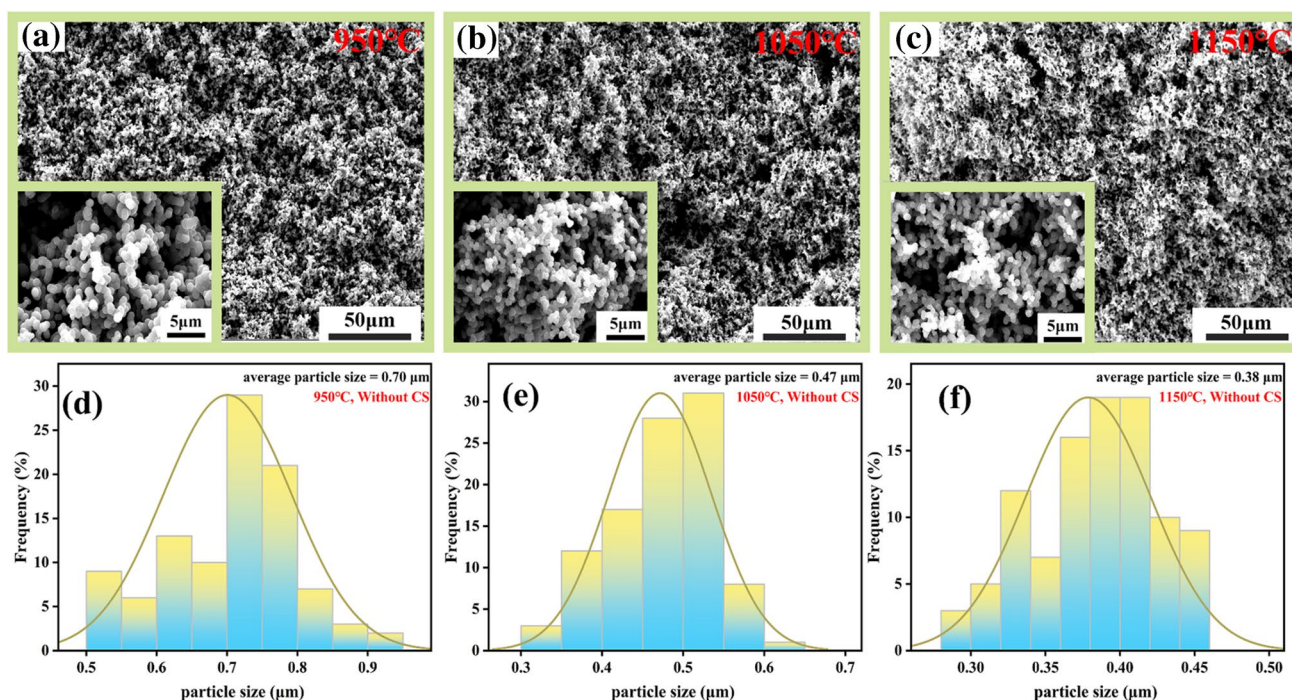


**Fig. 10** Effect of temperature on the microscopic morphology of coke: **a-c** Sem images. **d-f** Particle size distribution

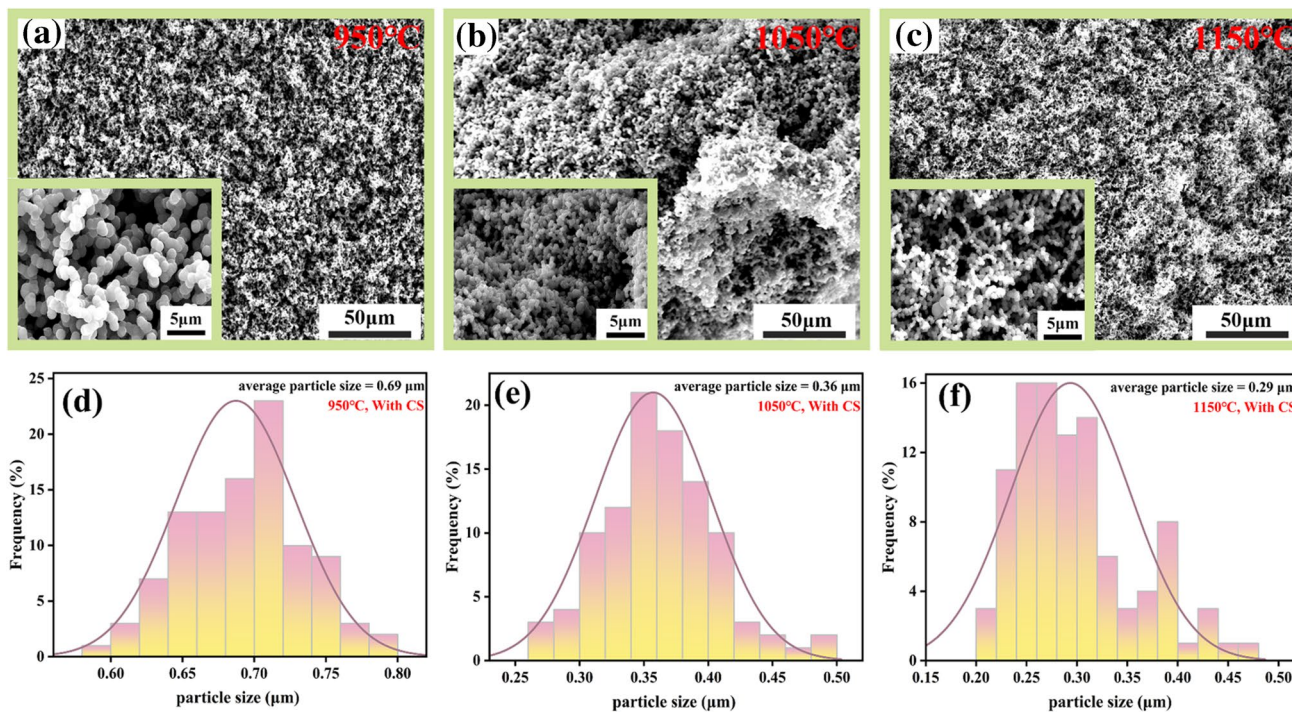


**Fig. 11** Effect of CS on the microscopic morphology of coke: **a-c** Sem images. **d-f** Particle size distribution

pathway of coke was not altered by the addition of CS. As can be seen in Fig. 10 (d-f), the average particle size of coke decreased as the pyrolysis temperature increased.

The average particle size of coke generally showed a decreasing trend under the effect of CS, from 0.69  $\mu\text{m}$  to 0.29  $\mu\text{m}$  (see Fig. 11 (d-f)). The decrease in particle



size is attributed to the high temperature conditions that accelerated the occurrence of the devolatilization reaction, resulting in the production of porous and fragmented coke [44]. Based on the results of Raman analysis in Sect. 3.3.1, it is shown that the concentration of small aromatic rings in coke is increasing, which may also be one of the reasons for the decrease in particle size. Meanwhile, the generation of volatiles can damage the internal structure of coke, resulting in a relatively rough surface of the formed coke.

### 3.5 Possible Pyrolysis Pathways of MO

Figure 12 shows the possible pyrolysis reaction pathways of MO in the presence of CS. Based on the results of Py-GC/MS experiments and combined with previous investigations, the pyrolysis process of methyl oleate was divided into three stages in this study. The first stage describes the primary decomposition reaction of MO. Some of the chemical bonds are broken and the cleavage products are fatty acids, ketenes and  $\text{CH}_3$  radical (pathway 1). The  $\text{CH}_3$  radical combines

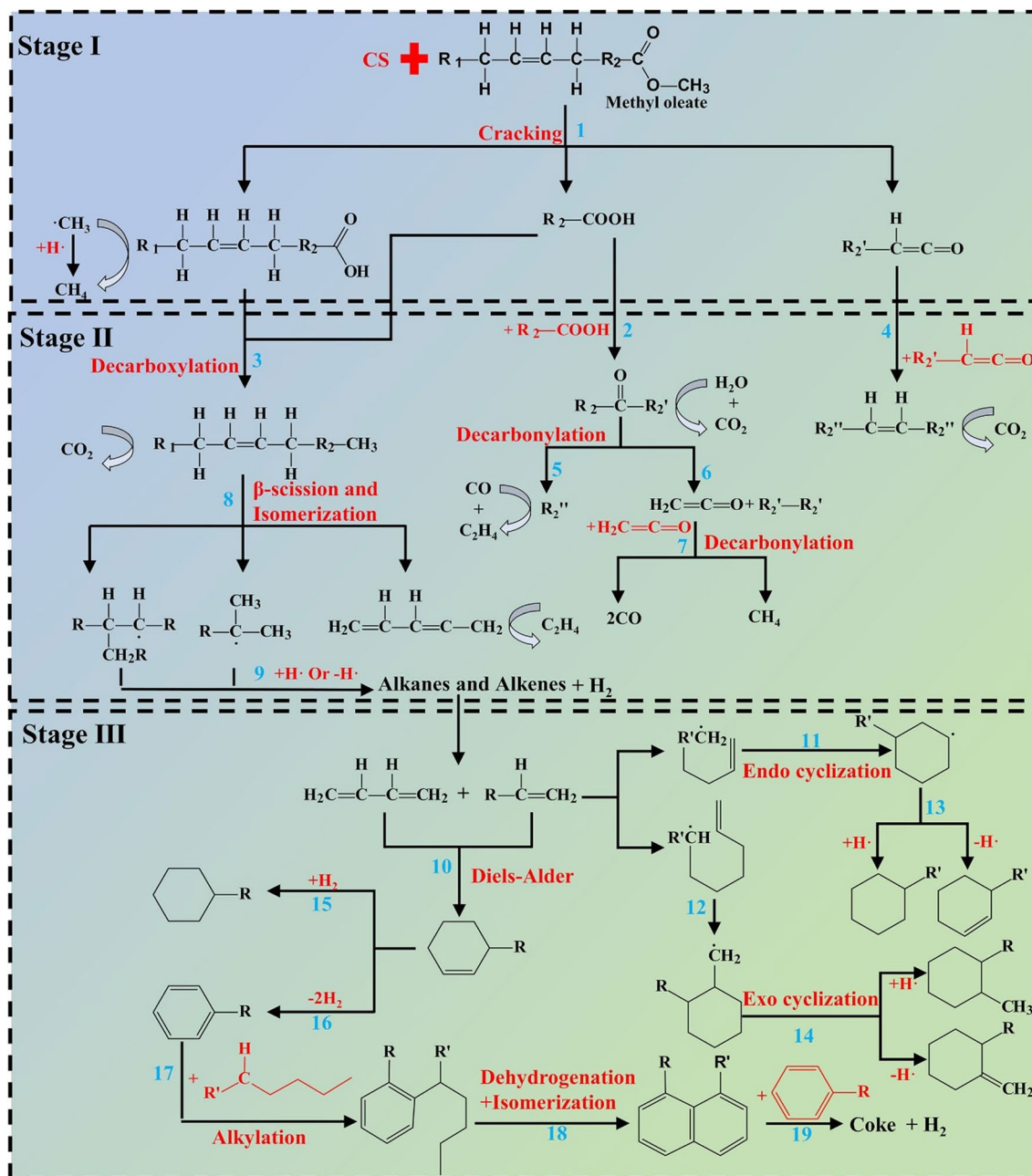


Fig. 12 Pyrolysis reaction pathway of MO in the presence of CS

with the hydrogen radical to form  $\text{CH}_4$ . The second stage primarily involves converting fatty acids and ketenes into hydrocarbons. Fatty acids undergo decarboxylation and ketonization reactions to form long-chain hydrocarbons, ketones,  $\text{CO}_2$ , and  $\text{H}_2\text{O}$  (pathways 2 and 3) [45]. Ketones can produce hydrocarbons,  $\text{CO}$  and  $\text{CO}_2$  through decarbonylation reactions (pathways 4–7). Subsequently, unsaturated hydrocarbons undergo  $\beta$ -scission and isomerization reactions (pathway 8), thereby converting into chain radicals, butadiene, and  $\text{C}_2\text{H}_4$  [46]. Chain radicals form alkanes and alkenes by absorbing or reducing hydrogen atoms, accompanied by the production of  $\text{H}_2$ . The third stage reflects the formation pathways of cyclic and aromatic hydrocarbons. Alkenes and alkenyl groups produce cyclic hydrocarbons through the Diels–Alder reaction (pathway 10) and cyclization reactions (pathways 11–14) [27]. Cyclic hydrocarbons form cycloalkanes and aromatic compounds through hydrogenation and dehydrogenation reactions (pathways 15 and 16). In this study, it was observed that as the temperature increased, the relative content of cyclic hydrocarbons decreased, while aromatic compounds increased. This is due to the fact that high temperature is conducive to the occurrence of dehydrogenation reactions [47]. Furthermore, aromatic compounds undergo alkylation to produce alkyl-substituted compounds (e.g., styrene and ethylbenzene). Then, PAHs are formed through dehydrogenation and isomerization (pathway 18) [48]. The generated MAHs and PAHs undergo further polymerization and dehydrogenation reactions at high temperatures, resulting in the formation of coke. Specific components of CS can promote the pyrolysis of MO to some extent. The presence of Cu, Fe and CaO positively affects the decarboxylation reaction (pathway 3) [34, 49]. Meanwhile, Cu and  $\text{Fe}^{3+}$  can effectively promote the decarbonylation reaction (pathways 4–7). Fe, metal oxides and CaO accelerate the breaking of C–C and C–H bonds, favoring the cleavage reaction in pathway 8. The presence of Cu, Fe, and alkaline oxides (CaO, MgO and ZnO) facilitates the dehydrogenation reaction (pathways 16, 18, and 19).

## 4 Conclusions

In this study, the thermal transformation behavior of MO was firstly investigated with the aim of elucidating the product evolution of rapid pyrolysis of MO. Py-GC/MS analysis indicated that the oxygenated compounds were first converted into hydrocarbons (alkenes and alkanes) as the temperature increased. Subsequently, the hydrocarbons were further converted to aromatics. TG-FTIR results demonstrated that the concentration of volatiles followed the sequence of  $\text{C-H} > \text{C}=\text{O} > \text{C-O-C} > -\text{CH}_2 > \text{C-H} > -(\text{CH}_2)_n$ . Furthermore, the changes of pyrolysis products and reaction characteristics of catalytic pyrolysis of MO by CS were analyzed. The GC

measurement results demonstrate that the primary components of the pyrolysis gas of MO are  $\text{H}_2$ ,  $\text{CH}_4$ ,  $\text{CO}$ ,  $\text{CO}_2$  and a small amount of  $\text{C}_2$  gases. The addition of CS promoted the production of  $\text{H}_2$  and  $\text{CO}$ . Two types of coke (without and with CS catalysis) were analyzed and characterized using FTIR, Raman and SEM. Raman analysis demonstrated that the total Raman area of coke decreased as the temperature increased. Moreover, the addition of CS also resulted in a decrease of the total Raman area. This illustrates that high temperatures and CS are favorable for the release of oxygen-containing structures during the pyrolysis process of MO. SEM analysis revealed that the coke was composed of small spherical particles and presented a coral-like structure. The particle size of coke exhibited a decreasing trend under the influence of CS. This investigation provides favorable information to explore the application of biodiesel in the copper smelting process, which is conducive to the sustainable development of the copper smelting industry.

**Supplementary Information** The online version contains supplementary material available at <https://doi.org/10.1007/s10562-024-04668-0>.

**Acknowledgements** This work is supported by the Yunnan Fundamental Research Projects (Grant No. 202302AO370018) and the National Natural Science Foundation of China (Grant No. U2102213, No. 51966007).

## References

1. Faizan M, Song H (2023) Critical review on catalytic biomass gasification: state-of-art progress, technical challenges, and perspectives in future development. *J Clean Prod* 408:137224. <https://doi.org/10.1016/j.jclepro.2023.137224>
2. Li S, Wu Y, Dao MU, Dragoi E, Xia C (2023) Spotlighting of the role of catalysis for biomass conversion to green fuels towards a sustainable environment: latest innovation avenues, insights, challenges, and future perspectives. *Chemosphere* 318:137954. <https://doi.org/10.1016/j.chemosphere.2023.137954>
3. Ghosh N, Rhithuparna D, Rokhum SL, Halder G (2023) Ethical issues pertaining to sustainable biodiesel synthesis over trans/esterification process. *Sustain Chem Pharm* 33:101123. <https://doi.org/10.1016/j.scp.2023.101123>
4. Kumar A, Singh VP, Srivastava A (2022) Quality biodiesel via biotransesterification from inedible renewable sources. *J Clean Prod* 379:134653. <https://doi.org/10.1016/j.jclepro.2022.134653>
5. Jin X, Li S, Ye H et al (2023) Investigation and optimization of biodiesel production based on multiple machine learning technologies. *Fuel* 348:128546. <https://doi.org/10.1016/j.fuel.2023.128546>
6. Ambat I, Srivastava V, Sillanpää M (2018) Recent advancement in biodiesel production methodologies using various feedstock: a review. *Renew Sust Energ Rev* 90:356–369. <https://doi.org/10.1016/j.rser.2018.03.069>
7. Singh D, Sharma D, Soni SL et al (2021) A comprehensive review of physicochemical properties, production process, performance and emissions characteristics of 2nd generation biodiesel feedstock: *jatropha curcas*. *Fuel* 285:119110. <https://doi.org/10.1016/j.fuel.2020.119110>
8. Suresh M, Jawahar CP, Richard A (2018) A review on biodiesel production, combustion, performance, and emission characteristics of non-edible oils in variable compression ratio diesel engine



- using biodiesel and its blends. *Renew Sust Energy Rev* 92:38–49. <https://doi.org/10.1016/j.rser.2018.04.048>
9. Maheshwari P, Haider MB, Yusuf M et al (2022) A review on latest trends in cleaner biodiesel production: role of feedstock, production methods, and catalysts. *J Clean Prod* 355:131588. <https://doi.org/10.1016/j.jclepro.2022.131588>
  10. Bayat A, Sadrameli SM, Towfighi J (2016) Production of green aromatics via catalytic cracking of canola oil methyl ester (CEM) using HZSM-5 catalyst with different Si/Al ratios. *Fuel* 180:244–255. <https://doi.org/10.1016/j.fuel.2016.03.086>
  11. Yu C, Yu S, Li L (2022) Upgraded methyl oleate to diesel-like hydrocarbons through selective hydrodeoxygenation over Mo-based catalyst. *Fuel* 308:122038. <https://doi.org/10.1016/j.fuel.2021.122038>
  12. Wang M, Feng C (2021) Towards a decoupling between economic expansion and carbon dioxide emissions in resources sector: a case study of China's 29 non-ferrous metal industries. *Resour Policy* 74:102249. <https://doi.org/10.1016/j.resourpol.2021.102249>
  13. Wang J, Liu W, Chen L, Li X, Wen Z (2023) Analysis of china's non-ferrous metals industry's path to peak carbon: a whole life cycle industry chain based on copper. *Sci Total Environ* 892:164454. <https://doi.org/10.1016/j.scitotenv.2023.164454>
  14. Zhou S, Wei Y, Li B, Wang H (2019) Cleaner recycling of iron from waste copper slag by using walnut shell char as green reductant. *J Clean Prod* 217:423–431. <https://doi.org/10.1016/j.jclepro.2019.01.184>
  15. Zuo Z, Yu Q, Wei M et al (2016) Thermogravimetric study of the reduction of copper slag by biomass. *J Therm Anal Calorim* 126(2):481–491. <https://doi.org/10.1007/s10973-016-5570-z>
  16. Kuang B, Zhang F, Yu Y et al (2023) Co-treatment of spent carbon anode and copper slag for reuse and the solidification of the constituent fluorine and heavy metals. *J Clean Prod* 383:135418. <https://doi.org/10.1016/j.jclepro.2022.135418>
  17. Du J, Zhang F, Hu J, Yang S, Liu H, Wang H (2022) Pyrolysis of rubber seed oil over high-temperature copper slag: gas and mechanism of coke formation. *Renew Energy* 185:1209–1220. <https://doi.org/10.1016/j.renene.2021.12.141>
  18. Dong N, Huo R, Liu M et al (2021) Chemical looping gasification of sewage sludge using copper slag modified by Nio as an oxygen carrier. *Chin J Chem Eng* 29:335–343. <https://doi.org/10.1016/j.cjche.2020.09.007>
  19. Pio DT, Tarelho LAC, Pinto RG et al (2018) Low-cost catalysts for in-situ improvement of producer gas quality during direct gasification of biomass. *Energy* 165:442–454. <https://doi.org/10.1016/j.energy.2018.09.119>
  20. Zhu Y, Zhou S, Wei Y, Li B, Wang H (2023) Insight into the function of waste cooking oil in the magnetite reduction process. *Renew Energy* 210:188–195. <https://doi.org/10.1016/j.renene.2023.04.068>
  21. Xu Z, Liu P, Xu G, Liu Q, He Z, Wang Q (2017) Bio-fuel oil characteristic from catalytic cracking of hydrogenated palm oil. *Energy* 133:666–675. <https://doi.org/10.1016/j.energy.2017.05.155>
  22. Wang X, Wang H, Jin X, Wang F, Shen B (2022) Synthetic strategies and performance of catalysts for pyrolytic production of alternative aviation fuels using non-edible lipids: a critical review. *Appl Catal A-Gen* 643:118769. <https://doi.org/10.1016/j.apcata.2022.118769>
  23. Shen T, Zhang F, Yang S et al (2023) Comprehensive study on the pyrolysis process of chestnut processing waste (chestnut shells): kinetic triplet, thermodynamic, in-situ monitoring of evolved gasses and analysis biochar. *Fuel* 331:125944. <https://doi.org/10.1016/j.fuel.2022.125944>
  24. Li H, Niu S, Lu C, Cheng S (2015) Comparative evaluation of thermal degradation for biodiesels derived from various feedstocks through transesterification. *Energy Convers Manag* 98:81–88. <https://doi.org/10.1016/j.enconman.2015.03.097>
  25. Abdul Jameel AG, Han Y, Brignoli O et al (2017) Heavy fuel oil pyrolysis and combustion: kinetics and evolved gases investigated by TGA-FTIR. *J Anal Appl Pyrolysis* 127:183–195. <https://doi.org/10.1016/j.jaap.2017.08.008>
  26. Xu Z, Cheng J, Song H et al (2020) Production of bio-fuel from plant oil asphalt via pyrolysis. *J Energy Inst* 93(5):1763–1772. <https://doi.org/10.1016/j.joei.2020.03.007>
  27. Beims RF, Botton V, Ender L et al (2018) Effect of degree of triglyceride unsaturation on aromatics content in bio-oil. *Fuel* 217:175–184. <https://doi.org/10.1016/j.fuel.2017.12.109>
  28. Tawalbeh M, Al-Othman A, Salamah T, Alkasrawi M, Martis R, El-Rub ZA (2021) A critical review on metal-based catalysts used in the pyrolysis of lignocellulosic biomass materials. *J Environ Manage* 299:113597. <https://doi.org/10.1016/j.jenvman.2021.113597>
  29. Zabeti M, Wan Daud WMA, Aroua MK (2009) Activity of solid catalysts for biodiesel production: a review. *Fuel Process Technol* 90(6):770–777. <https://doi.org/10.1016/j.fuproc.2009.03.010>
  30. Ochoa A, Bilbao J, Gayubo AG, Castaño P (2020) Coke formation and deactivation during catalytic reforming of biomass and waste pyrolysis products: a review. *Renew Sust Energy Rev* 119:109600. <https://doi.org/10.1016/j.rser.2019.109600>
  31. Chen X, Che Q, Li S et al (2019) Recent developments in lignocellulosic biomass catalytic fast pyrolysis: strategies for the optimization of bio-oil quality and yield. *Fuel Process Technol* 196:106180. <https://doi.org/10.1016/j.fuproc.2019.106180>
  32. Qiu B, Yang C, Shao Q, Liu Y, Chu H (2022) Recent advances on industrial solid waste catalysts for improving the quality of bio-oil from biomass catalytic cracking: a review. *Fuel* 315:123218. <https://doi.org/10.1016/j.fuel.2022.123218>
  33. Chen F, Zhang F, Yang S, Liu H, Wang H, Hu J (2021) Investigation of pyrolysis kinetics, thermodynamics, product characteristics and reaction mechanism of rubber seed oil. *Energy Convers Manag* 244:114535. <https://doi.org/10.1016/j.enconman.2021.114535>
  34. Zhang C, Hu X, Guo H et al (2018) Pyrolysis of poplar, cellulose and lignin: effects of acidity and alkalinity of the metal oxide catalysts. *J Anal Appl Pyrolysis* 134:590–605. <https://doi.org/10.1016/j.jaap.2018.08.009>
  35. Kan T, Strezov V, Evans TJ (2016) Lignocellulosic biomass pyrolysis: a review of product properties and effects of pyrolysis parameters. *Renew Sust Energy Rev* 57:1126–1140. <https://doi.org/10.1016/j.rser.2015.12.185>
  36. Hatefirad P, Hosseini M, Tavasoli A (2022) Effect of Fe/Cu catalysts supported on zeolite/active carbon hybrid on bio-oil quality derived from catalytic pyrolysis of granular bacteria biomass. *Fuel* 312:122870. <https://doi.org/10.1016/j.fuel.2021.122870>
  37. Zhang X, Sun L, Chen L et al (2014) Comparison of catalytic upgrading of biomass fast pyrolysis vapors over CaO and Fe(III)/CaO catalysts. *J Anal Appl Pyrolysis* 108:35–40. <https://doi.org/10.1016/j.jaap.2014.05.020>
  38. Das SK, Ghosh GK, Avasthe RK, Sinha K (2021) Compositional heterogeneity of different biochar: effect of pyrolysis temperature and feedstocks. *J Environ Manage* 278:111501. <https://doi.org/10.1016/j.jenvman.2020.111501>
  39. Omoriyekomwan JE, Tahmasebi A, Zhang J, Yu J (2017) Formation of hollow carbon nanofibers on bio-char during microwave pyrolysis of palm kernel shell. *Energy Convers Manag* 148:583–592. <https://doi.org/10.1016/j.enconman.2017.06.022>
  40. Shao Y, Guizani C, Grosseau P, Chaussy D, Beneventi D (2018) Biocarbons from microfibrillated cellulose/lignosulfonate precursors: a study of electrical conductivity development during slow pyrolysis. *Carbon* 129:357–366. <https://doi.org/10.1016/j.carbon.2017.12.037>
  41. Zhao Y, Feng D, Zhang Y, Huang Y, Sun S (2016) Effect of pyrolysis temperature on char structure and chemical speciation of

- alkali and alkaline earth metallic species in biochar. *Fuel Process Technol* 141:54–60. <https://doi.org/10.1016/j.fuproc.2015.06.029>
42. Du J, Zhang F, Hu J, Yang S, Liu H, Wang H (2023) Co-pyrolysis of industrial hemp stems and waste plastics into biochar-based briquette: product characteristics and reaction mechanisms. *Fuel Process Technol* 247:107793. <https://doi.org/10.1016/j.fuproc.2023.107793>
43. Zhang L, Li T, Quyn D, Dong L, Qiu P, Li C (2015) Formation of nascent char structure during the fast pyrolysis of mallee wood and low-rank coals. *Fuel* 150:486–492. <https://doi.org/10.1016/j.fuel.2015.02.066>
44. Das SK, Ghosh GK, Avasthe R, Sinha K (2021) Morpho-mineralogical exploration of crop, weed and tree derived biochar. *J Hazard Mater* 407:124370. <https://doi.org/10.1016/j.jhazmat.2020.124370>
45. Seifi H, Sadrameli SM (2016) Bound cleavage at carboxyl group-glycerol backbone position in thermal cracking of the triglycerides in sunflower oil. *J Anal Appl Pyrolysis* 121:1–10. <https://doi.org/10.1016/j.jaap.2016.06.006>
46. Cheah YW, Salam MA, Sebastian J et al (2023) Upgrading of triglycerides, pyrolysis oil, and lignin over metal sulfide catalysts: a review on the reaction mechanism, kinetics, and catalyst deactivation. *J Environ Chem Eng* 11(3):109614. <https://doi.org/10.1016/j.jece.2023.109614>
47. Zhai Y, Feng B, Yuan W, Ao C, Zhang L (2018) Experimental and modeling studies of small typical methyl esters pyrolysis: methyl butanoate and methyl crotonate. *Combust Flame* 191:160–174. <https://doi.org/10.1016/j.combustflame.2017.12.033>
48. Xu J, Long F, Jiang J et al (2019) Integrated catalytic conversion of waste triglycerides to liquid hydrocarbons for aviation biofuels. *J Clean Prod* 222:784–792. <https://doi.org/10.1016/j.jclepro.2019.03.094>
49. Jiraroj D, Jirarattanapochai O, Anutrasakda W, Samec JSM, Tungasmita DN (2021) Selective decarboxylation of biobased fatty acids using a ni-fsm-16 catalyst. *Appl Catal B* 291:120050. <https://doi.org/10.1016/j.apcatb.2021.120050>

**Publisher's Note** Springer Nature remains neutral with regard to jurisdictional claims in published maps and institutional affiliations.

Springer Nature or its licensor (e.g. a society or other partner) holds exclusive rights to this article under a publishing agreement with the author(s) or other rightsholder(s); author self-archiving of the accepted manuscript version of this article is solely governed by the terms of such publishing agreement and applicable law.